Journal of
Ceramic Science
and Technology

J. Ceram. Sci. Technol., **13** [1] 45-64 (2022)
DOI: 10.4416/JCST2021-00021
available online at: http://www.ceramic-science.com

RE_2SiO_5 (RE=Er, Gd, Y, Yb), Which is More Suitable for the Top-Coat of EBCs: A Problem Clarification via Finite Element Simulation Study

X.W. Sun[1, 2], X. Zhong[2], Z.C. Hu[1], Y. Liu[2], Y. Yang*[1], L. Wang*[2]

[1]Key Lab. for New Type of Functional Materials in Hebei Province, School of Materials Science and Engineering, State Key Laboratory of Reliability and Intelligence of Electrical Equipment, Tianjin Key Laboratory of Materials Laminating Fabrication and Interface Control Technology, Hebei University of Technology 300401, Tianjin, China
[2]Integrated Computational Materials Research Centre, Shanghai Institute of Ceramics, Chinese Academy of Sciences, Shanghai, 201899, China

received December 21, 2021; received in revised form March 7, 2022; accepted March 16, 2022

Abstract

As an important surface protection method, environmental barrier coatings (EBCs) have been applied in the aerospace industry. In order to prepare advanced EBCs with low residual stress, high bonding strength, excellent anti-oxidation resistance and long service lifetime by means of APS (Atmospheric Plasma Spraying), the finite element method (FEM) has been used to design and optimize the structure of the EBCs, thereby saving on experimental costs and improving investigation efficiency. The current work focuses on the influence of the top-coat layer (RE_2SiO_5) and the thickness of the corresponding layer on the residual stress of the EBCs. The simulation results revealed that an over-thick top-coat resulted in high residual stress and the thickness of the top-coat should not exceed 170 µm. The simulation results showed that the residual stresses in Er_2SiO_5 and Y_2SiO_5 were significantly lower than those in Yb_2SiO_5 and Gd_2SiO_5, the maximum axial stress of Er_2SiO_5, Gd_2SiO_5, Y_2SiO_5, Yb_2SiO_5 is 167 MPa, 191 MPa, 165 MPa, 294 MPa, respectively. It could be concluded that the most suitable top-coat consisted of Y_2SiO_5 with a thickness of 140 µm, as this produces high-quality coatings based on the current simulation results. The experiment results showed that Y_2SiO_5 and Er_2SiO_5 had fewer cracks, indicating a low stress level (142.6 MPa ±4 MPa), which was consistent with the simulation results.

Keywords: Finite element simulation, environmental barrier coating systems, residual stress, atmospheric plasma spraying, failure mechanism

I. Introduction

The development of the aviation industry has accelerated the development of aircraft engines [1] Hence, the improvement of the thrust-to-weight ratio for engines should be a primary consideration [2]. The realization of a high thrust-to-weight ratio requires light structural materials with a high service temperature [3]. The limit for the melting point of Ni-based super-alloys (1 150 °C) was difficult to break through [4]. So, Ni-based super-alloys have been replaced by SiC_f/SiC composites with lower density, high service temperature and many other excellent properties [5]. But SiC_f/SiC composites are susceptible to environmental corrosion at high temperatures [6]. EBCs are therefore used to extend the working life of SiC_f/SiC. The function of EBCs is to protect the SiC_f/SiC composites in severe environments, and directly prevent or reduce high-temperature damage to the surface of SiC_f/SiC composites [7].

The development of EBCs has gone through three stages [8]. The first generation of EBCs is composed of yttria-stabilized zirconia (YSZ) and mullite. However, owing to the large difference in the CTE, cracks are initiated and propagated during thermal cycling, causing layers to peel off and shortening the lifetime of EBCs. The second-generation EBCs are composed of mullite + BSAS (1-xBaO-xSrO-Al_2O_3-2SiO_2,0≤x≤1). The disadvantage of the second-generation EBCs is that the maximum service temperature is too low (<1 300 °C) [9–12]. The volatilization rate of the coating is significantly increased at a high service temperature, which leads to rapid failure of the coating. At present, silicate is used for third-generation EBCs, but this needs to be explored and investigated. The advantages of third-generation EBCs are that they have excellent phase stability, better chemical compatibility and water resistance, but there is large difference in the CTE between two adjacent layers. The lifetime of EBCs is directly related to residual stress, which results in crack initiation and propagation at the inner boundary of the ceramic layer or along the interface between the adjacent layers.

Multilayer EBCs are now attracting a great deal of attention. Bradley T. Richards *et al.* [13] have investigated

* Corresponding author: L.Wang@mail.sic.ac.cn
co-corresponding author: yangyonghebut@163.com, yangyong@hebut.edu.cn

an Yb_2SiO_5 coating fabricated by means of APS and found it has good anti-steam recession and anti-oxygen corrosion at 1 400 °C. Edge delamination of the coating system has been observed. This is caused by bending of the delaminated region to relax the stress in the surface layer developed by TGO and Yb_2SiO_5 during the cooling step of each thermal cycle. B.J. Harder *et al.* [14] have investigated doped aluminosilicate coatings to assess their stability on a SiC/SiC-melt-infiltrated substrate. They used a numerical model to compare the stress results and analyzed the strain and phase evolution as a function of multi-layer depth and temperature. They found that the phase transformation in the top-coat promoted the healing of cracks in the EBCs and reduced stress levels in the underlying layers, while the addition of SAS($SrAl_2Si_2O_8$) to the interlayer reduced stresses, but did not stop cracks from forming. Bradley T. Richards *et al.* [15] used optimized air plasma spraying parameters to deposit a tri-layer $Yb_2SiO_5/Al_6Si_2O_{13}/Si$ on substrates to improve interface adherence and reduce the concentration of defects. During the cooling process, tensile stresses developed in the ytterbium monociliate layer since its CTE exceeded that of the substrate. These stresses drove vertical mud cracks that underwent crack branching either within the $Al_6Si_2O_{13}$(mullite) layer or at one of its interfaces. Xin Zhong *et al.* [16] have evaluated and compared the microstructure evolution, thermal expansion, thermal conductivity and thermal shock resistance properties of the plasma-sprayed X1-Gd_2SiO_5, X2-Y_2SiO_5 and X2-Er_2SiO_5 coatings based on experimental measurement and theoretical exploration, and found that the X2-Y_2SiO_5 and X2-Er_2SiO_5 coatings with lower thermal mismatch stresses presented much better thermal shock resistance than that of the X1-Gd_2SiO_5 coating.

High residual stress was generated during the preparation of the APS-coating [14–18]. When the stress on a component exceeds its yield strength, the component will produce plastic deformation. Generally, the formation of residual stresses includes thermal mismatch stress, impact stress, quenching stress and phase transition stress [19–21]:

(1) The quenching stress and impact stress: the high-temperature molten particles are quenched to the temperature of the substrate when they contact with the substrate in the spraying process. When the coating is sprayed onto a colder substrate, quenching stress is generated in the ceramic coating. Quenching stress is caused by the rapid shrinkage of the sprayed splash sheet from the processing temperature to the substrate temperature as it rapidly cools. At the same time, the un-melted particles contact the substrate in the process of coating fabrication, some high-temperature particles will rebound. Therefore, impact stress is generated.

(2) Stress-induced phase transformation: phase transformation stress is caused by the phase transformation that may occur in the air thermal spraying process. And the phase transition stress is generated during the solidification of liquid particles and solid-phase transition.

(3) Thermal mismatch stress: the CTE of adjacent layers are different. Thermal stress is induced owing to the thermal mismatch of the CTE between the ceramic layer and the substrate. Thermal stress results from difference in the CTE between the coating and substrate as the substrate and coating cool together from the spraying state to room temperature.

But the main residual stress is from the thermal mismatch stress for EBCs [22]. So, the discussion will focus on the damage to the top-coat caused by thermal mismatch stress. The current research is urgently needed to improve EBCs, to avoid lengthy experiments, high cost and because of the absence of systematic research. In addition, the delamination of coatings is mainly caused by residual stress, the residual stress mainly originating at the interface of the EBCs [18–20]. So, it is necessary to optimize the preparation process for EBCs to accelerate assessment of the magnitude of residual stress values. This is an important approach to reduce residual stress in the preparation of high-quality EBCs. Numerical simulation is a method which uses a computer as the investigation tool. Actual physical experiments usually require long experimental periods, incur high costs, and, in some cases, experiments are difficult to observe or realize, so numerical simulation is a good alternative [23–26]. Numerical simulations have certain advantages, such as low cost, short experimental periods and safe operation. Hence, numerical simulations have played an irreplaceable role in the field of scientific investigations [27]. Although some experimental parameters cannot be measured by direct experiments, they can be verified based on indirect data and inferences by means of numerical simulation, which can also speed up experimental progress and improve experimental efficiency. FEM is a kind of numerical simulation which uses mathematics to solve partial differential equations in order to obtain approximate solutions. FEM can help us save on experimental costs and time, and accelerate the process of EBC design and new material development, as shown in Fig. 1. Therefore, FEM can be used to analyze the residual stress in EBCs prepared by means of APS. The focus is on the effect of a different composition and different thickness of the top-coat, which would provide useful guidance for the preparation of EBCs with excellent performance. A suitable material for use as the top-coat for EBCs is selected and the corresponding thickness optimized.

II. Methods and Procedures

(1) Material parameters

Since the thermo-physical properties of materials are dependent on temperature, the data of the thermo-physical properties of materials at different temperatures can be considered comprehensively. This facilitates the acquisition of more accurate calculation results. The material properties of Er_2SiO_5, Gd_2SiO_5, Y_2SiO_5, Yb_2SiO_5, $Yb_2Si_2O_7$ and mullite are shown in Table 1, Table 2, Table 3, Table 4, Table 5 and Table 6 [16,18,28], respectively.

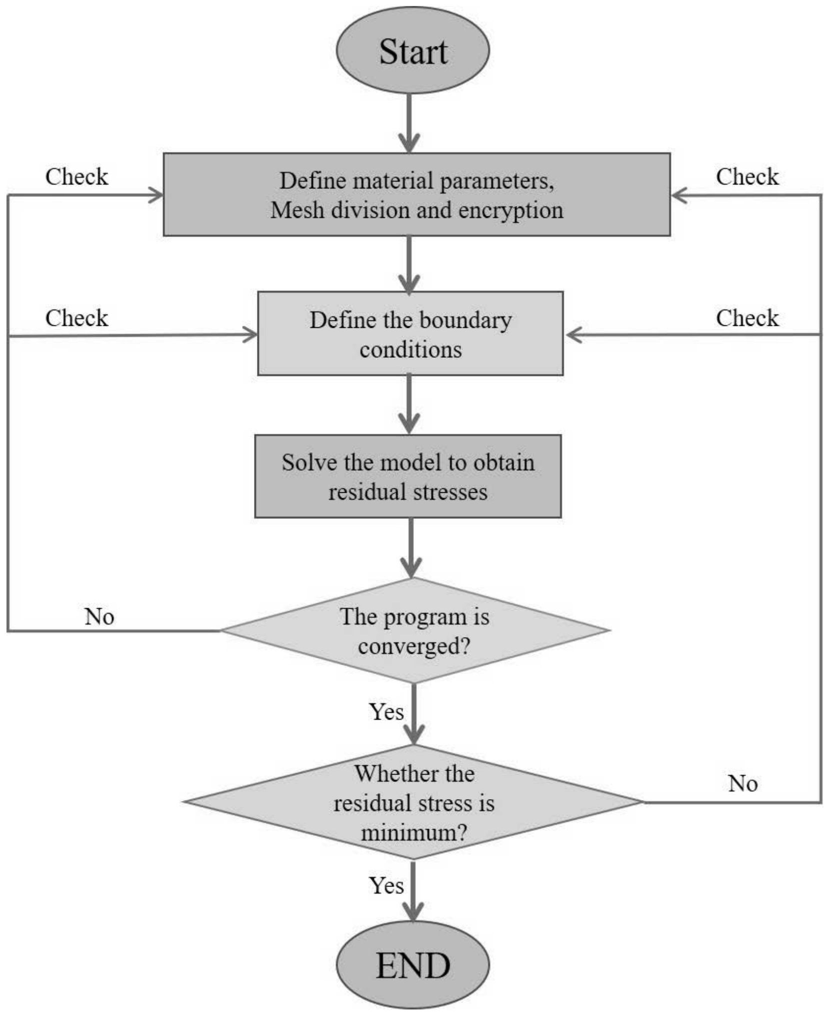

Fig. 1: The flowchart showing finite element simulation of residual stress in EBCs.

Table 1: Material properties of Yb_2SiO_5 used in the finite element simulation.

T (°C)	k(W/m·K)	c(J/g·K)	α (K^{-1})	E(GPa)	v	ρ (10^3kg/m^3)
25	0.67901	0.29435	6.83e-6	97.3	0.23	7.07
100	0.68767	0.35339	6.92e-6	97.3	0.23	7.07
200	0.68057	0.3958	7.01e-6	97.3	0.23	7.07
300	0.66716	0.42091	7.09e-6	97.3	0.23	7.07
400	0.66661	0.43817	7.15e-6	97.3	0.23	7.07
500	0.68348	0.45136	7.19e-6	97.3	0.23	7.07
600	0.70652	0.46225	7.22e-6	97.3	0.23	7.07
700	0.73434	0.47172	7.25e-6	97.3	0.23	7.07
800	0.76126	0.48028	7.28e-6	97.3	0.23	7.07
900	0.79459	0.48823	7.31e-6	97.3	0.23	7.07
1000	0.8454	0.49574	7.34e-6	97.3	0.23	7.07
1100	0.93955	0.50295	7.39e-6	97.3	0.23	7.07
1200	1.12579	0.50993	7.44e-6	97.3	0.23	7.07

Table 2: Material properties of Y_2SiO_5 used in the finite element simulation.

T (°C)	k(W/m·K)	c(J/g·K)	α (K^{-1})	E(GPa)	v	ρ ($10^3 kg/m^3$)
25	0.53594	0.390402475	5.25e-6	72.94	0.2	4.16
100	0.6101	0.465585306	4.99e-6	72.94	0.2	4.16
200	0.64893	0.523467898	5.36e-6	72.94	0.2	4.16
300	0.63962	0.56114733	5.63e-6	72.94	0.2	4.16
400	0.61081	0.589675494	5.86e-6	72.94	0.2	4.16
500	0.5742	0.613463539	6.03e-6	72.94	0.2	4.16
600	0.54115	0.634552743	6.17e-6	72.94	0.2	4.16
700	0.51964	0.653993112	6.29e-6	72.94	0.2	4.16
800	0.50906	0.672369569	6.40e-6	72.94	0.2	4.16
900	0.51669	0.690028919	6.49e-6	72.94	0.2	4.16
1000	0.53248	0.707187363	6.58e-6	72.94	0.2	4.16
1100	0.56019	0.723985366	6.69e-6	72.94	0.2	4.16
1200	0.5853	0.740517398	6.79e-6	72.94	0.2	4.16

Table 3: Material properties of Gd_2SiO_5 used in the finite element simulation.

T (°C)	k(W/m·K)	c(J/g·K)	α (K^{-1})	E(GPa)	v	ρ ($10^3 kg/m^3$)
25	0.58078	0.292235062	6.98e-6	75.15	0.24	6.23
100	0.6197	0.340654239	7.58e-6	75.15	0.24	6.23
200	0.62743	0.377193013	8.07e-6	75.15	0.24	6.23
300	0.60112	0.400368252	8.40e-6	75.15	0.24	6.23
400	0.5462	0.417490314	8.65e-6	75.15	0.24	6.23
500	0.49192	0.431476988	8.82e-6	75.15	0.24	6.23
600	0.44226	0.443678493	8.96e-6	75.15	0.24	6.23
700	0.408	0.454789364	9.06e-6	75.15	0.24	6.23
800	0.39705	0.465196502	9.17e-6	75.15	0.24	6.23
900	0.41145	0.475129304	9.28e-6	75.15	0.24	6.23
1000	0.44694	0.484730777	9.39e-6	75.15	0.24	6.23
1100	0.50175	0.494093835	9.50e-6	75.15	0.24	6.23
1200	0.56438	0.503280964	9.59e-6	75.15	0.24	6.23

Table 4: Material properties of Er_2SiO_5 used in the finite element simulation.

T (°C)	k (W/m·K)	c(J/g·K)	α (K^{-1})	E(GPa)	v	ρ (10^3kg/m^3)
25	0.61112	0.298941516	5.20e-6	74.5	0.22	6.59
100	0.6086	0.341219377	5.20e-6	74.5	0.22	6.59
200	0.60237	0.375254603	5.50e-6	74.5	0.22	6.59
300	0.56607	0.39863756	5.79e-6	74.5	0.22	6.59
400	0.52374	0.417195441	6.02e-6	74.5	0.22	6.59
500	0.48446	0.433254059	6.22e-6	74.5	0.22	6.59
600	0.45166	0.447889692	6.38e-6	74.5	0.22	6.59
700	0.43387	0.461655964	6.51e-6	74.5	0.22	6.59
800	0.43325	0.474861281	6.63e-6	74.5	0.22	6.59
900	0.44496	0.487688497	6.73e-6	74.5	0.22	6.59
1000	0.47015	0.500251607	6.84e-6	74.5	0.22	6.59
1100	0.50287	0.512624672	6.96e-6	74.5	0.22	6.59
1200	0.54008	0.524857501	7.06e-6	74.5	0.22	6.59

Table 5: Material properties of Yb_2SiO_7 used in the finite element simulation.

T (°C)	k (W/m·K)	c(J/g·K)	α (K^{-1})	E(GPa)	v	ρ (10^3kg/m^3)
25	0.8646	0.33131	3.12e-6	67.49	0.27	5.67
100	0.8235	0.4106	3.24e-6	67.49	0.27	5.67
200	0.77638	0.46592	3.39e-6	67.49	0.27	5.67
300	0.74114	0.49719	3.55e-6	67.49	0.27	5.67
400	0.70406	0.51758	3.70e-6	67.49	0.27	5.67
500	0.68188	0.53233	3.84e-6	67.49	0.27	5.67
600	0.67816	0.54387	3.98e-6	67.49	0.27	5.67
700	0.69951	0.55344	4.12e-6	67.49	0.27	5.67
800	0.75459	0.56175	4.26e-6	67.49	0.27	5.67
900	0.84526	0.5692	4.40e-6	67.49	0.27	5.67
1000	0.97298	0.57606	4.53e-6	67.49	0.27	5.67
1100	1.14562	0.58249	4.66e-6	67.49	0.27	5.67
1200	1.36782	0.5886	4.78e-6	67.49	0.27	5.67

Table 6: Material properties of mullite used in the finite element simulation.

T (°C)	k(W/m·K)	c(J/g·K)	α (K^{-1})	E(GPa)	v	ρ (10^3kg/m^3)
	2.5	0.76	5.30e-6	110	0.28	2.65

(2) FEM model and boundary conditions

According to the schematic shown in Fig. 2, as for cylindrical specimens, simplification to a 2D model is possible [29], the temperature of the system can be described as follows:

$$\rho c_p \frac{\partial T}{\partial t} = k\left[\frac{\partial^2 T}{\partial y^2}+\frac{\partial^2 T}{\partial r^2}+\frac{1}{r}\frac{\partial T}{\partial t}\right] \qquad (1)$$

where ρ is the density (kg/m^3), c_p is the specific heat (kJ/(kg·K)), T is the system temperature (K), t is the time (s), $\partial T/\partial t$ is the normal temperature gradient (K/m), and k is the thermal conductivity (W/(m·K)).

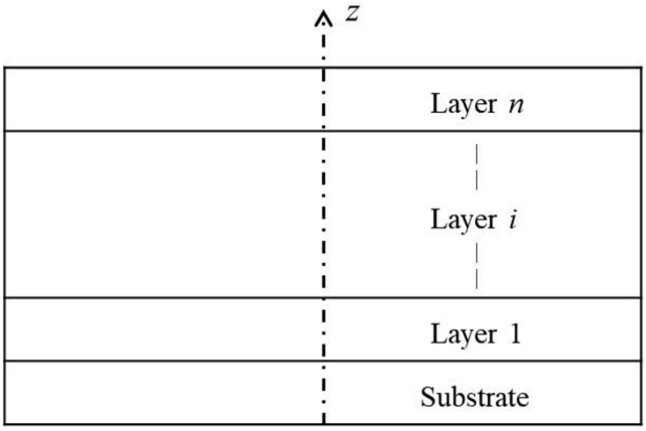

Fig. 2: Schematic illustration of the calculation model for the multilayer coating.

The temperature field of the specimen is obtained depending on the thermodynamic conditions. The thermal strain and stress can then be determined based on the numerical analysis of temperature fields according to the thermal elasticity theory. The third boundary condition applied to this model is expressed as:

$$-k\left.\frac{\partial T}{\partial n}\right|_{\tau_c} = h\left(T_w - T_f\right) \qquad (2)$$

where τ_c is the time constant (s), h is the heat transfer coefficient (W/(m^2·K)), T_f is the ambient temperature (K), and T_w is the temperature of the specimen (K).

The stress and strain must satisfy the following equations: Balance equation

$$\left.\begin{aligned} \frac{\partial \sigma_r}{\partial r}+\frac{\partial \tau_{zr}}{\partial y}+\frac{\sigma_r-\sigma_0}{r}+f_r=0 \\ \frac{\partial \tau_{ry}}{\partial r}+\frac{\partial \sigma_y}{\partial y}+\frac{\tau_{rz}}{r}+f_y=0 \end{aligned}\right\} \qquad (3)$$

Physical equation:

$$\begin{Bmatrix}\sigma_r\\ \sigma_\theta\\ \sigma_y\\ \tau_{ry}\end{Bmatrix} = \frac{E(1-\mu)}{(1+\mu)(1-2\mu)}\begin{bmatrix}1 & A_1 & A_1 & 0\\ A_1 & 1 & A_1 & 0\\ A_1 & A_1 & 1 & 0\\ 0 & 0 & 0 & A_2\end{bmatrix}\begin{bmatrix}\varepsilon_r-(1+\mu)\alpha\Delta T\\ \varepsilon_\theta-(1+\mu)\alpha\Delta T\\ \varepsilon_y-(1+\mu)\alpha\Delta T\\ \gamma_{ry}\end{bmatrix} \qquad (4)$$

where σ is the normal stress (Pa), τ is the shearing stress (Pa), f is the component of the body force (N/m^3), ε is the linear strain (m), γ is the shear strain (m), E is the Young's modulus (MPa), μ is Poisson's ratio, α is the thermal expansion coefficient (1/K), ΔT is the variation of temperature (K), $A_1 = \frac{\mu}{(1-\mu)}$, and $A_2 = \frac{(1-2\mu)}{2(1-\mu)}$.

In the current work, ANSYS APDL is used for simulations by means of FEM with the following assumptions:

(1) This model is regarded as a transient-state problem. All layers are uniformly isotropic and each layer is free of defects. The interface between two adjacent layers is flat with no cracks or pores.

(2) The upper surface of the coating transfers heat only with air by convection and other edges are adiabatic, the thermal radiation is not considered.

(3) The adjacent layer is assumed to be linearly elastic. The axisymmetric model is chosen to reduce the data processing time and improve the calculation accuracy. In this mode, the overall coating structure is designed as four sections, SiC_f/SiC substrate (9 mm), Si bond-coat (100 μm), $Yb_2Si_2O_7$ interlayer (100 μm) and top-coat (50–200 μm) including Er_2SiO_5, Gd_2SiO_5, Y_2SiO_5 and Yb_2SiO_5 as shown in Fig. 3. In this work, PLANE13 is used for meshing and procedures. The interfaces of adjacent layers are refined to improve the accuracy of the simulation results.

The constraint conditions are applied to the axial and bottom of the model, with $u_x = 0$ in the horizontal direction on the left side and $u_y = 0$ in the vertical direction of the bottom. And the symmetrical boundary conditions were applied. The multi-point coupling (MPC) constraint was imposed on the right side of the model, which is regarded as the geometric boundary condition. The initial temperature of the SiC layer is set to 1 175 °C [15] (temperature at the end of spraying, when the coating has been completely formed on the substrate) and that of the interlayer, bond-coat and top-coat is set to 1 940 °C, 2 300 °C and 2 000 °C, respectively (this is the melting point or phase transformation point for coatings.) and the cooling time is 1 800 s from initial temperature to room temperature (25 °C) [16]. The convection coefficient between the outer surface of the sample and air is set to 100 W/(m^2·K) [17]. The equipment for the preparation of EBCs was an A-2000 automatic atmospheric plasma spraying system (Sulzer Metco, Switzerland), which consists of the F4-MB spray gun and the S3 robot made by ABB, USA, and the Twin10–2 double cartridge powder feeding system. The plasma-generating gas is argon and hydrogen, and the powder-feeding carrier gas is argon. The spraying power is 43 kW, the flow rate of the argon, hydrogen and carrier gas are 38 L·min^{-1}, 12 L·min^{-1} and 3 L·min^{-1}. The principle and measurement of surface residual stress using XRD is shown in Fig. 3(c) and Fig. 3 (d), respectively.

III. Results and Discussion

The stress of four EBC systems are compared in this section, the stress plot of the different EBC systems is discussed, as shown in Fig. 4. The maximum radial tensile stress (*Sx*), the maximum axial tensile stress (*Sy*), the maximum shear stress (*Sxy*) and the maximum equivalent stress (*Seqv*) is 98.3 MPa, 63.9 MPa, 10.0 MPa and 99.7 MPa, respectively. It can be found that the residual stresses of the samples are principally concentrated on the top-coat.

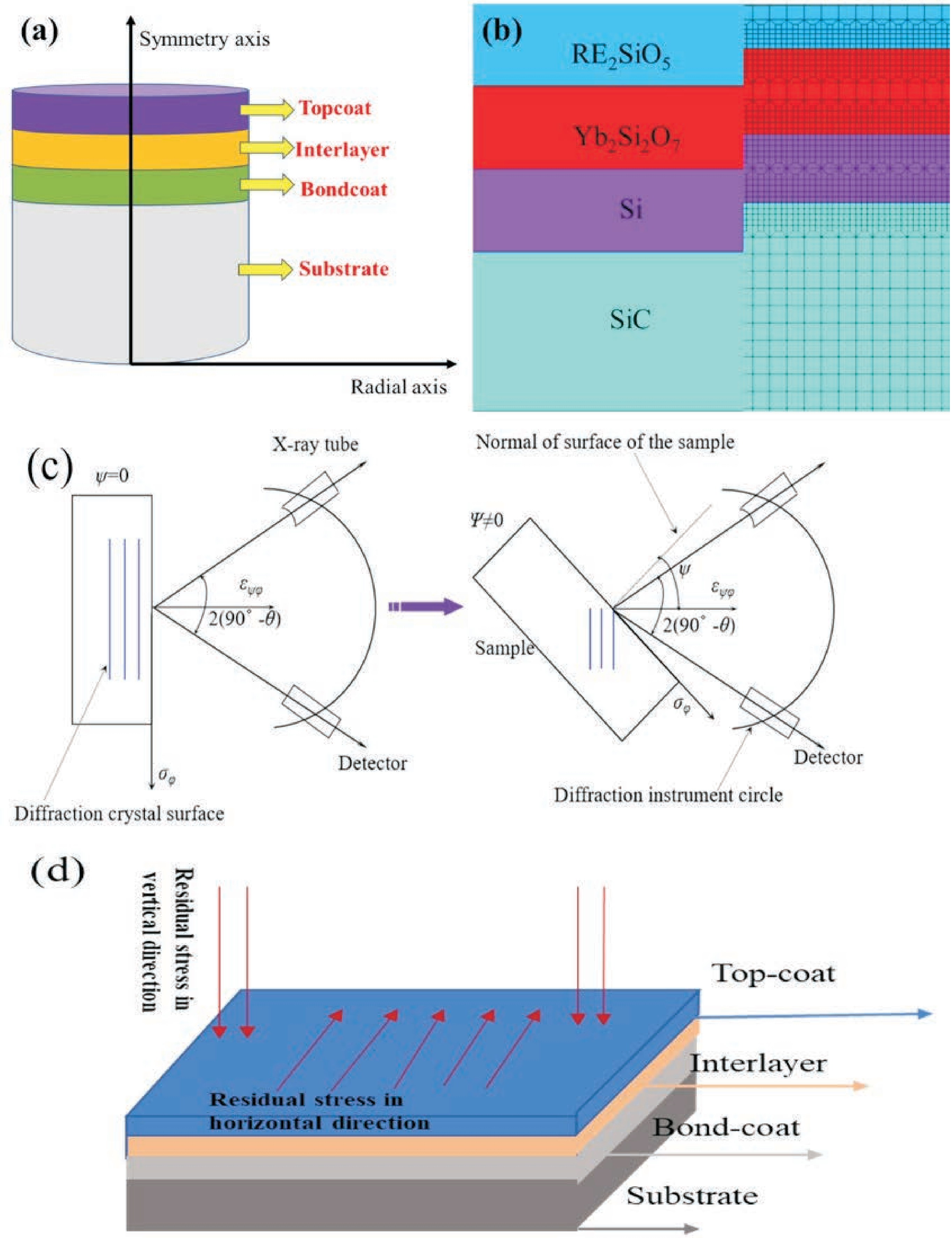

Fig. 3: (a) Finite element model of EBCs, (b) The finite element mesh, (c) Principle of measurement of surface residual stress using XRD, (d) Diagram showing the direction of residual stress for EBCs.

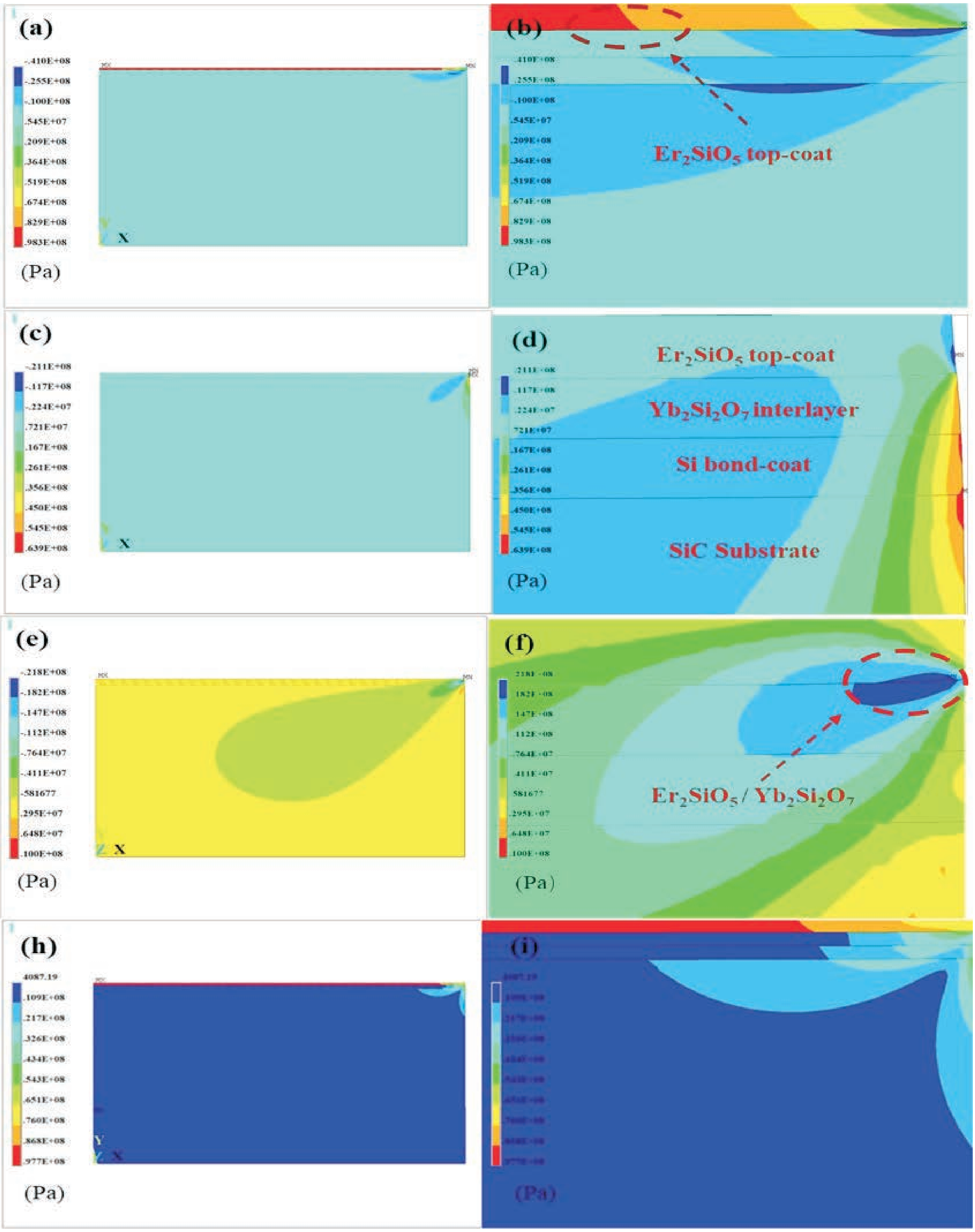

Fig. 4: Residual stress of Er_2SiO_5: (a) *Sx*, (c) *Sy*, (e) *Sxy*, (h) *Seqv* and (b), (d), (f), (i) show the magnified region.

However, compared with the whole sample, the residual stresses in the substrate are relatively low. The residual stress is transferred to the top-coat once the preparation process is finished and the entire samples have cooled to room temperature. The various stresses indicator was intersected at the edge of the coating, which indicated that the chaotic stress zone could be restricted.

Generally, the influence of the composition and thickness of the top-coat of EBCs on its residual stress is crucial [30]. In previous EBCs, mullite was used as the interlayer and monatomic Si was used as the bond-coat. The mullite interlayer prevents oxygen atoms penetrating into the substrate and protect the substrate against oxidization in the harsh service environment. However, the existence of a mullite interlayer caused new problems, owing to the thermo-physical properties of mullite being different from those of the SiC substrate, which leads to the coatings peeling off easily. Therefore, it is necessary to verify whether this viewpoint is correct. As shown in Fig. 5(a), the axial stress and radial stress of Yb_2SiO_5 and Gd_2SiO_5 are significantly higher than that of Er_2SiO_5 and Y_2SiO_5, but their shear stress is close to each other. And the maximum axial stress of Er_2SiO_5, Gd_2SiO_5, Y_2SiO_5, Yb_2SiO_5 is 167 MPa, 191 MPa, 165 MPa, 294 MPa, respectively. When the $Yb_2Si_2O_7$ interlayer was replaced with mullite, it was found that the residual stress of the coating had significantly increased when the increase in axial stress was the most evident, as shown in Fig. 5(b). Thus, the disadvantage of mullite is that it increases the possibility of the coating peeling, which is consistent with the reason for the failure of YSZ. So, an $Yb_2Si_2O_7$ interlayer is the better choice than a mullite interlayer. The top layer affects the performance of the coating more than the middle layer. And this work also focuses on the composition and structure of the top-coat. The more specific analysis and discussion is detailed in the subsequent section.

The residual stress as a function of thickness is shown for each silicate in Fig. 6. Fig. 6(a), Fig. 6(c) and Fig. 6(d) show the radial stress, axial stress, shear stress and equivalent stress, respectively. As can be seen from Fig. 6, the variation of residual stress of EBCs is consistent with the increase in the coating thickness. The radial stress and equivalent stress have limited variation, which could be regarded as being unchanged. The shear stress has exhibited an increasing tendency and only reduced by 80 ~ 110 μm. The axial stress showed a linear increasing tendency with increasing thickness. With the increase in the thickness of the top-coat, the axial stress increased by about 88 %, so there was large increase in the axial stress, and the increase in the axial stress probably caused the adhesion strength between the coating and the substrate to deteriorate. It can be seen from Fig. 6, the residual stress of Er_2SiO_5 and Y_2SiO_5 is almost equal, which can be attributed to their similar coefficients of thermal expansion. Although the average coefficient of thermal expansion of Yb_2SiO_5 is lower than that of Gd_2SiO_5, the stress of Gd_2SiO_5 is higher than that of Yb_2SiO_5. This is mainly because that the average thermal conductivity and average specific heat capacity of Yb_2SiO_5 were lower than those of Gd_2SiO_5. The same decrease in temperature would result in lower strain, thus the stress is lower. Lower residual stress significantly lengthened the service lifetime of the coatings.

The stress concentration in the coating is mainly concentrated at the interface between the adjacent layers. So, building paths at the interface and analyzing the stress distribution along the paths can help us understand the failure mechanism of coatings better, as shown in Fig. 7. The residual stress in the adjacent layers is shown in Fig. 8 – Fig. 13. Two factors for the failure mechanism of the coating are discussed in detail, the composition and thickness of the top-coat.

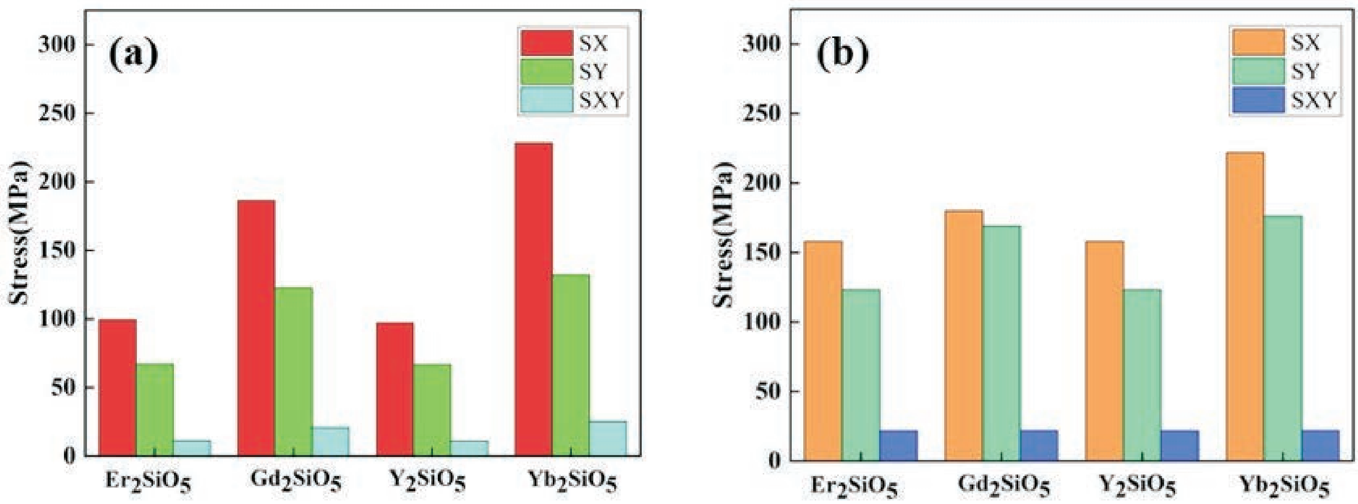

Fig. 5: Residual stress of $Yb_2Si_2O_7$ and mullite: (a) $Yb_2Si_2O_7$, (b) mullite.

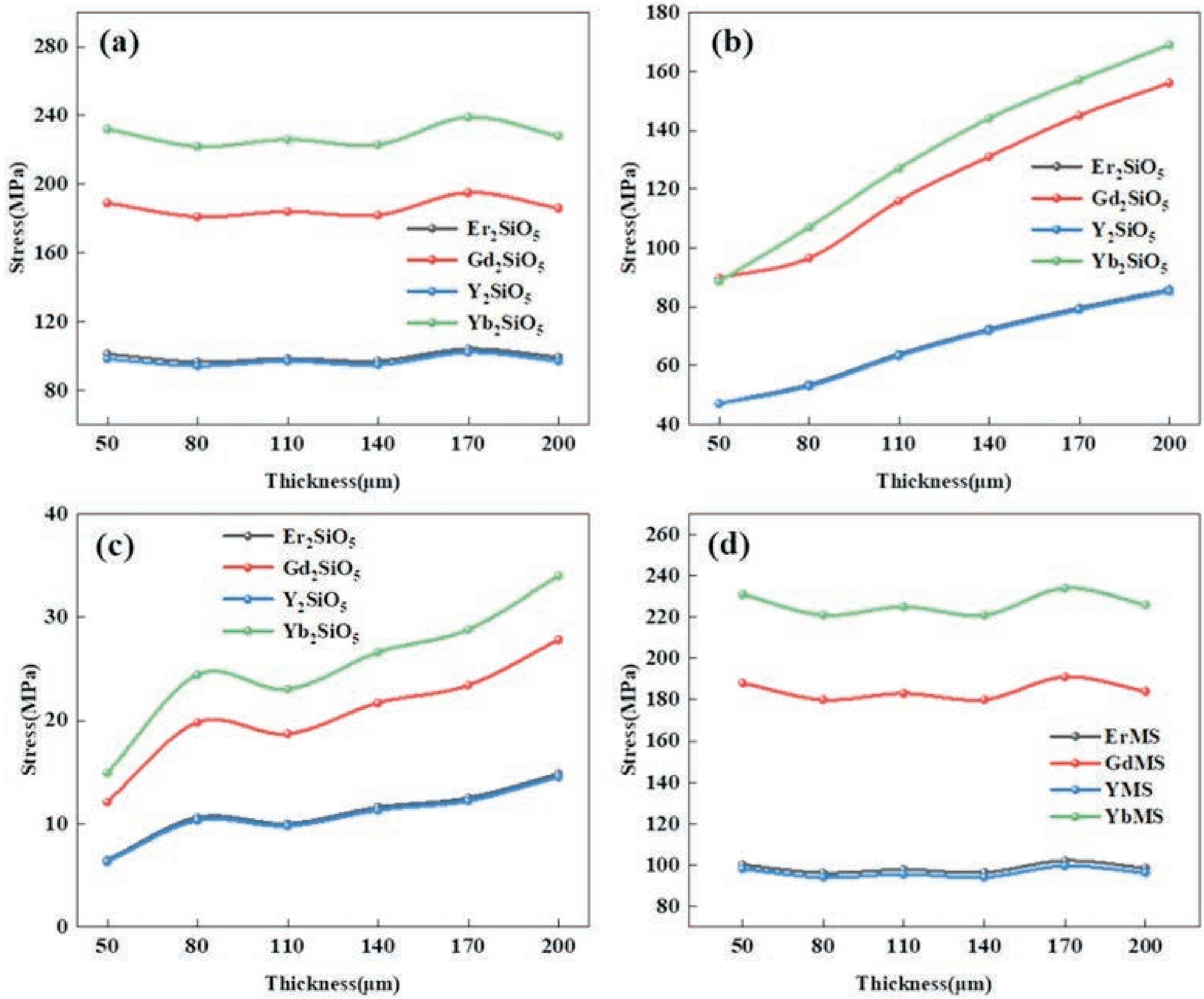

Fig. 6: Residual stress of silicate material: (a)*Sx*, (b)*Sy*, (c)*Sxy*, (d)*Seqv*.

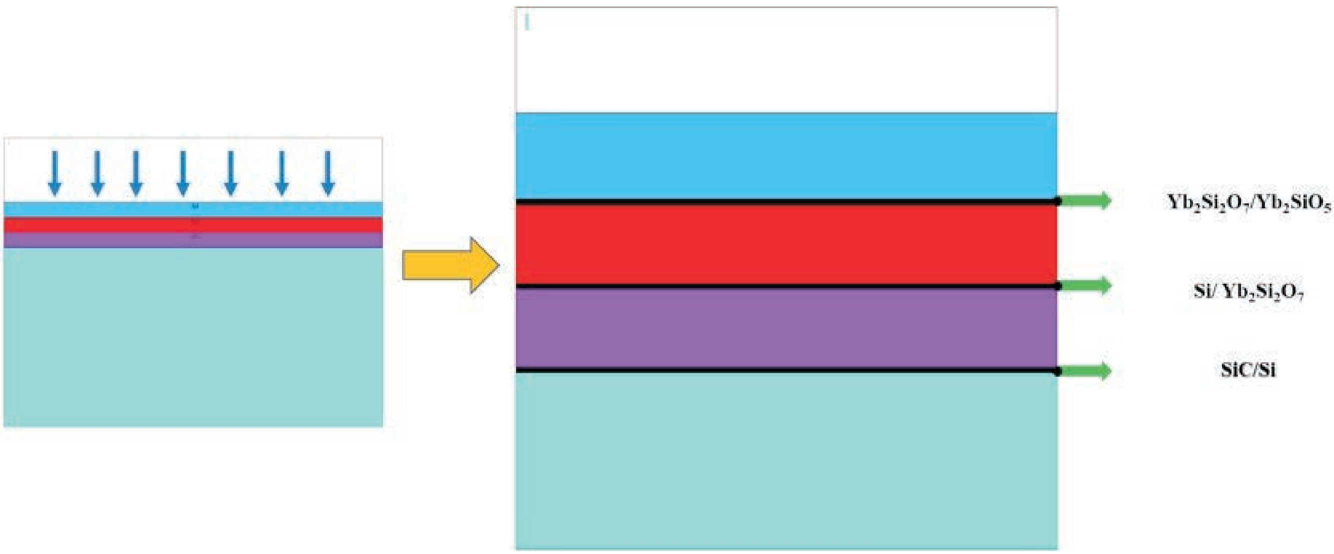

Fig. 7: Definition of paths for the FEM model.

(1) Effect of the thickness on residual stress of the EBCs

In order to consider the effect of the thickness of the RE_2SiO_5 top-coat on the residual stress, the coating system for $Yb_2Si_2O_7/Yb_2SiO_5$ is selected for discussion, as shown in Fig. 8, Fig. 9 and Fig. 10. The interfacial stress of Si/SiC is considered, Fig. 8(a), Fig. 8(b), Fig. 8(c) and Fig. 8(d) show the radial stress, axial stress, shear stress and equivalent stress, respectively. It was found that the residual stress increased with increasing thickness of the top-coat in the range of 50 μm to 200 μm. There was a mutation of stress at 14 ~ 16 mm along the specific path where the stress increases and decreases rapidly. As shown in Fig. 9 for the $Yb_2Si_2O_7$/Si interface, Fig. 9(a), Fig. 9(b), Fig. 9(c) and Fig. 9(d) show the radial stress, axial stress, shear stress and equivalent stress, respectively. It could be found that the trend of stress variation was the same as that of the Si/SiC interface, except that the magnitude of stress was reduced by about 10 % on average. This was because that the larger strain is generated at the inner boundary of the top-coat, which resulted in the stress level slightly decreasing. As shown in Fig. 10 for the $Yb_2SiO_5/Yb_2Si_2O_7$ interface, Fig. 10(a), Fig. 10(b), Fig. 10(c) and Fig. 10(d) show the radial stress, axial stress, shear stress and equivalent stress, respectively. The trend of the variation of axial stress and shear stress for $Yb_2SiO_5/Yb_2Si_2O_7$ was the same as that of the $Yb_2Si_2O_7$/Si interface, but the radial stress and equivalent stress show a large difference to that of the $Yb_2Si_2O_7$/Si interface. The radial stress at this interface was much larger at 0 ~ 14 mm and decreased at 14 ~ 16 mm. And the residual stress of the top-coat for the thickness with 170 and 200 μm were much higher than that for 50 – 140 μm. This indicated that a huge accumulation of radial stress was on the surface of coatings. Also, the increase in the thickness of the top-coat significantly increased the residual stresses at all interfaces. The presence of excessive tensile stress led to the development and growth of cracks, which would be extremely detrimental to the coating lifetime. The radial stress at the $Yb_2SiO_5/Yb_2Si_2O_7$ interface increased with the thickness of the top-coat, but at the thickness of 170 μm and 200 μm of the top-coat, there was a sharp jump in stress, as shown in Fig. 10. The fact is that the greater thickness results in stress concentration at the surface of the top-coat.

Based on the stress distribution of the key interfaces, it can be found that the stress concentrations at all interfaces occurred at the edge of the top-coat. There are chaotic residual stresses at 14 ~ 16 mm of the coating, and the stresses are intertwined with each other, which is very likely to lead to the growth of defects. In addition, the damage of the coating was also induced here, which led to the cracking [31]. An appropriate thickness is helpful for this situation, from the findings of this experiment, the thickness of the coating on the surface should not exceed 170 μm. The thickness of coatings had a significant impact on the interfacial stress of coatings, which affected the quality and protective effect of the coating. Therefore, in the actual preparation process, the factors such as fabrication technology, the actual performance specifications and production cost should be taken into account in order to select an appropriate thickness for engineering applications [32].

(2) Optimization of the composition of EBCs

The selection of different materials has played an important role in designing and optimizing the structure of EBCs for the purposes of aviation [33–34]. The residual stress of Er_2SiO_5, Gd_2SiO_5, Y_2SiO_5 and Yb_2SiO_5 should be compared and analysed in detail. The thickness of the top-coat is set to 110 μm, as shown in Fig. 11, Fig. 12 and Fig. 13. As for the interface of Si/SiC, Fig. 11(a), Fig. 11(b), Fig. 11(c) and Fig. 11(d) shows the radial stress, axial stress, shear stress and equivalent stress, respectively. A large difference in the stress was found with a different top-coat, the stress of Gd_2SiO_5 and Yb_2SiO_5 being significantly higher than that of Er_2SiO_5 and Y_2SiO_5. The stress is concentrated at 14 ~ 16 mm for each layer, where the stress is heterogeneous at the $Yb_2Si_2O_7$/Si interface, as shown in Fig. 12. Fig. 12(a), Fig. 12(b), Fig. 12(c) and Fig. 12(d) show the radial stress, axial stress, shear stress and equivalent stress, respectively. The $Yb_2Si_2O_7$/Si interface was basically the same as the Si/SiC interface, but with a slight decrease. This is essentially the same as that of Fig. 9 with the same reason. As shown in Fig. 12 for $Yb_2SiO_5/Yb_2Si_2O_7$ interface, Fig. 13(a), Fig. 13(b), Fig. 13(c) and Fig. 13(d) show the radial stress, axial stress, shear stress and equivalent stress, respectively. It can be found that the relationship between stress and path is consistent with Fig. 10. The larger radial stress was located at the $Yb_2SiO_5/Yb_2Si_2O_7$ interface. There is a large mutation in stress at 14 ~ 16 mm where the residual stress increases and decreases rapidly. The residual stress in Er_2SiO_5 and Y_2SiO_5 was significantly lower than that in Yb_2SiO_5 and Gd_2SiO_5, and the detailed rule for residual stress is $Yb_2SiO_5 > Gd_2SiO_5 > Er_2SiO_5 > Y_2SiO_5$. This was mainly due to the inextricable relationship with the thermophysical properties of the materials. The substrate and the bond-coat are stress relaxed, while the interlayer and the top-coat are the stress-concentration zone as shown in Fig. 11, Fig. 12 and Fig. 13, which is due to the growth of stress as the thickness of top-coat increases and the residual stress concentrates in the top-coat. This was because that the CTE of the substrate matches well with the layers at high temperature, and the coating with the larger CTE would produce higher strain during the cooling process. Then the stress between layers would increase so that cracks can easily be formed in the coating, leading to a decrease in the bonding strength. The material parameters in the adjacent layers should be as similar as possible so that the coating with this structure has higher bonding strength [35–36]. If the thermophysical parameters of the above materials are compared, it can be seen that the thermal-physical parameters of Er_2SiO_5 and Y_2SiO_5 were more similar to SiC even at elevated temperature, this was the main reason for the lower residual stress of the coatings when the top-coat is prepared with Er_2SiO_5 and Y_2SiO_5. From this experiment, it was concluded that the combination of Er_2SiO_5 or Y_2SiO_5 with the SiC substrate led to a lower residual stress for EBCs, which dramatically reduced the possibility of coating failure.

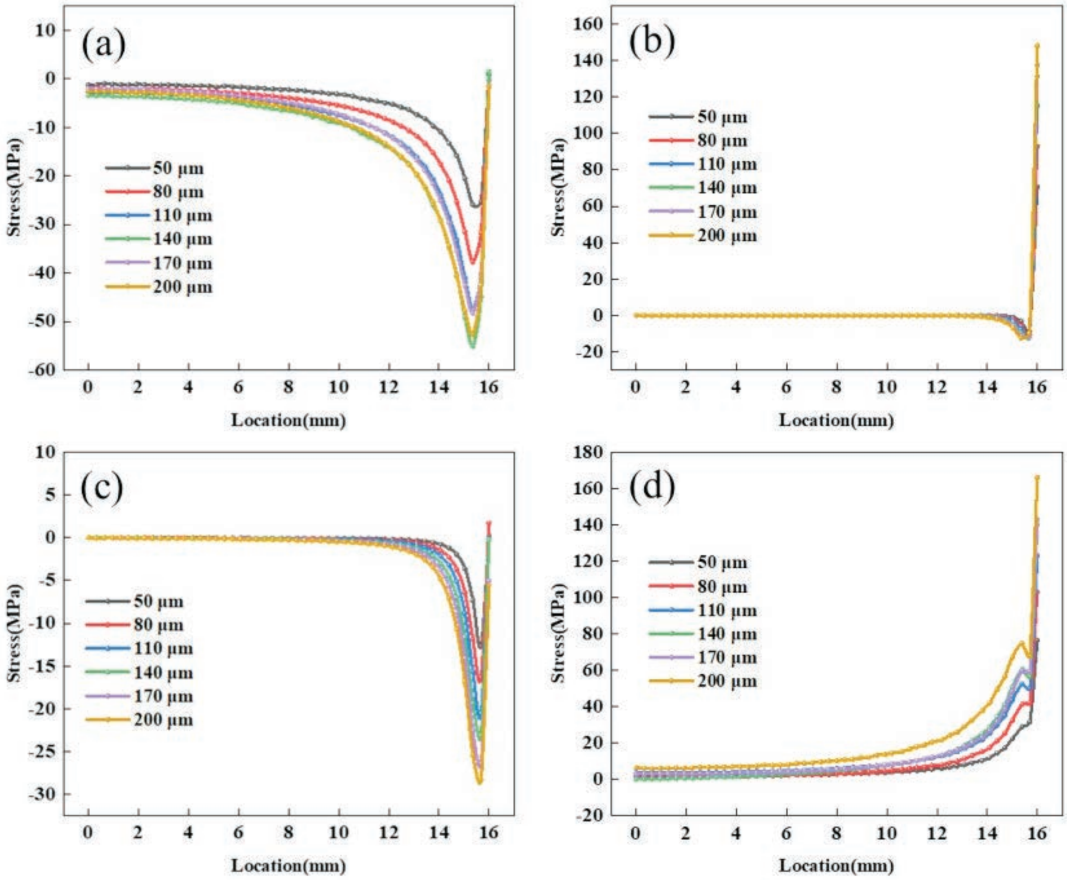

Fig. 8: Residual stress as the function of the location along the radial direction with different thickness for the Si/SiC interface of the top-coat: (a)*Sx*, (b)*Sy*, (c)*Sxy*, (d)*Seqv*.

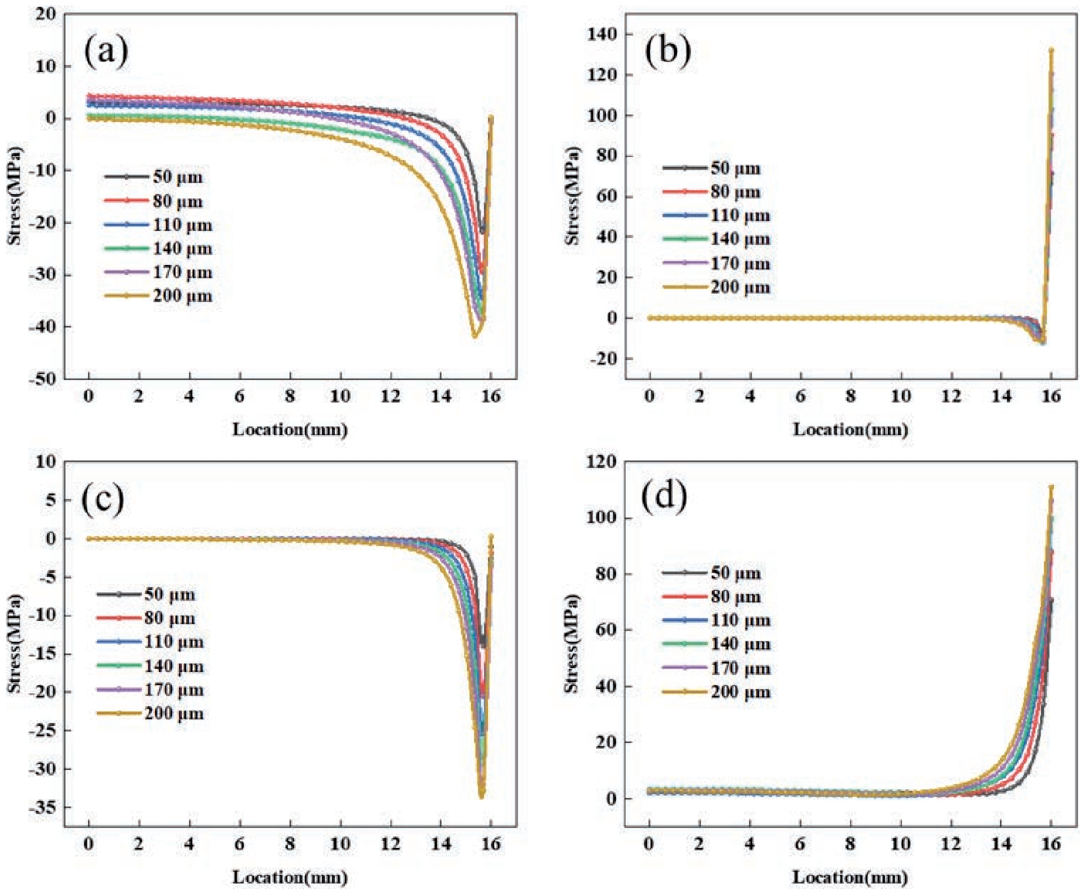

Fig. 9: Residual stress as the function of the location along the radial direction with different thickness for the $Yb_2Si_2O_7$/Si interface of the top-coat: (a)*Sx*, (b)*Sy*, (c)*Sxy*, (d)*Seqv*.

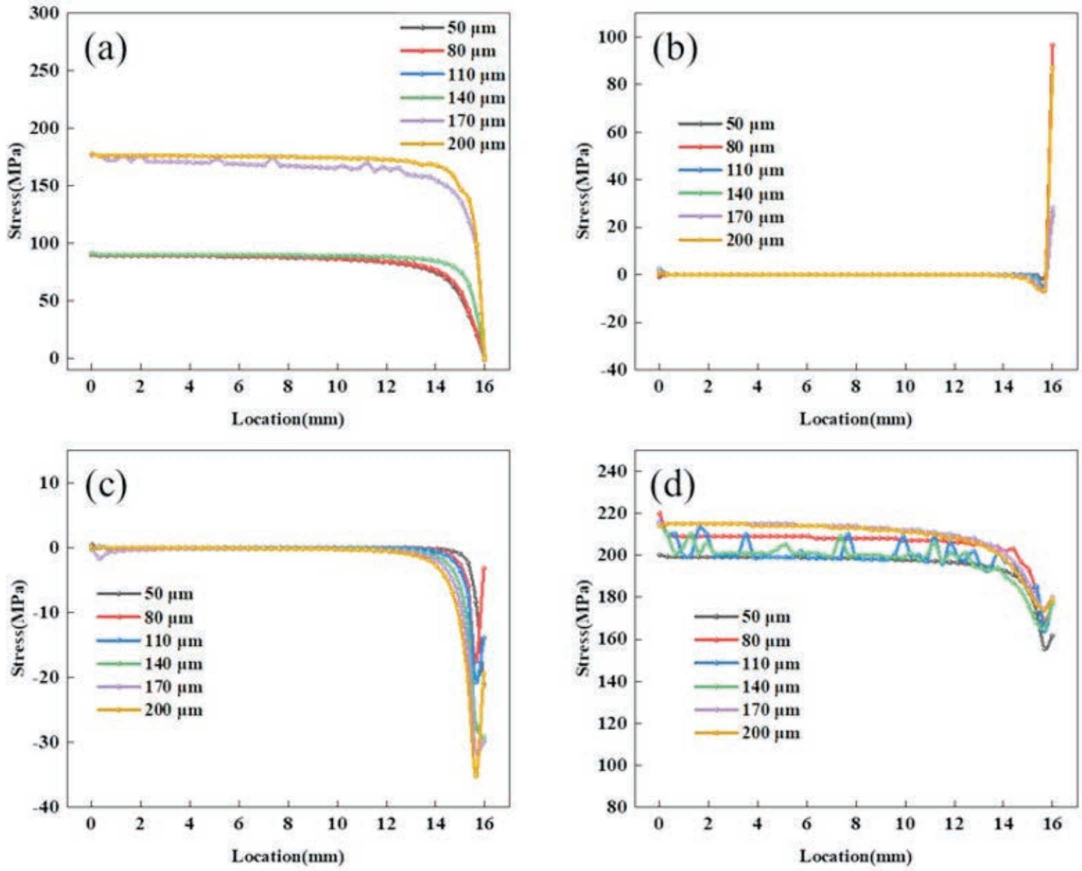

Fig. 10: Residual stress as the function of the location along the radial direction with different thickness for the $Yb_2SiO_5/Yb_2Si_2O_7$ interface of the top-coat: (a)*Sx*, (b)*Sy*, (c)*Sxy*, (d)*Seqv*.

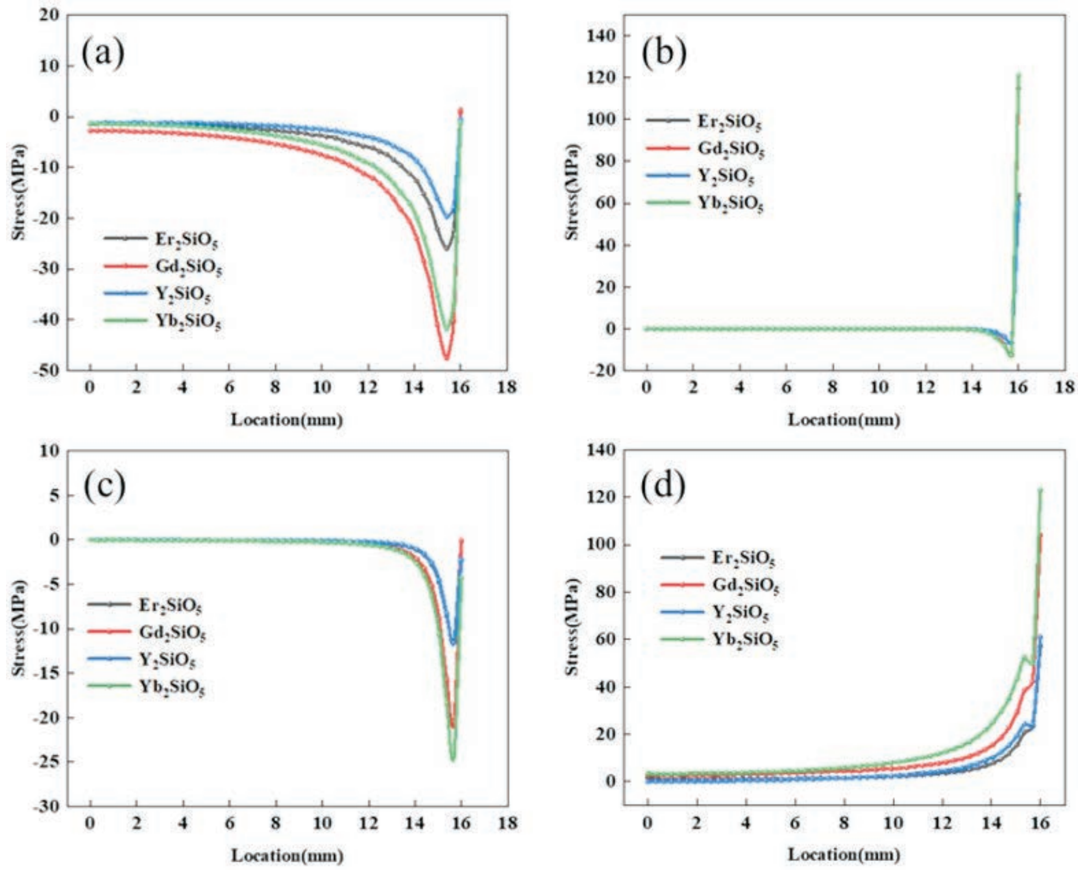

Fig. 11: Residual stress as the function of the location along the radial direction with a 110-μm top-coat for the Si/SiC interface: (a)*Sx*, (b)*Sy*, (c)*Sxy*, (d)*Seqv*.

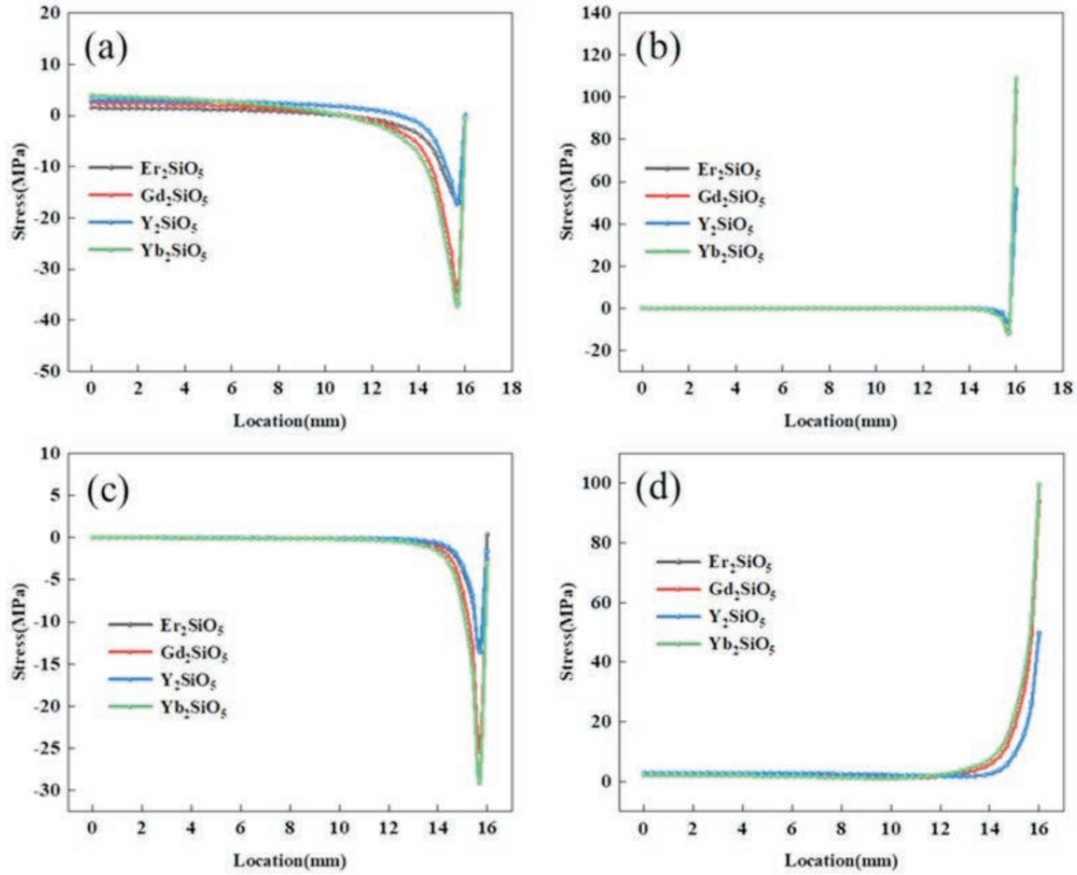

Fig. 12: Residual stress as the function of the location along the radial direction with a 110-µm top-coat for the $Yb_2Si_2O_7$/Si interface: (a)*Sx*, (b)*Sy*, (c)*Sxy*, (d)*Seqv*.

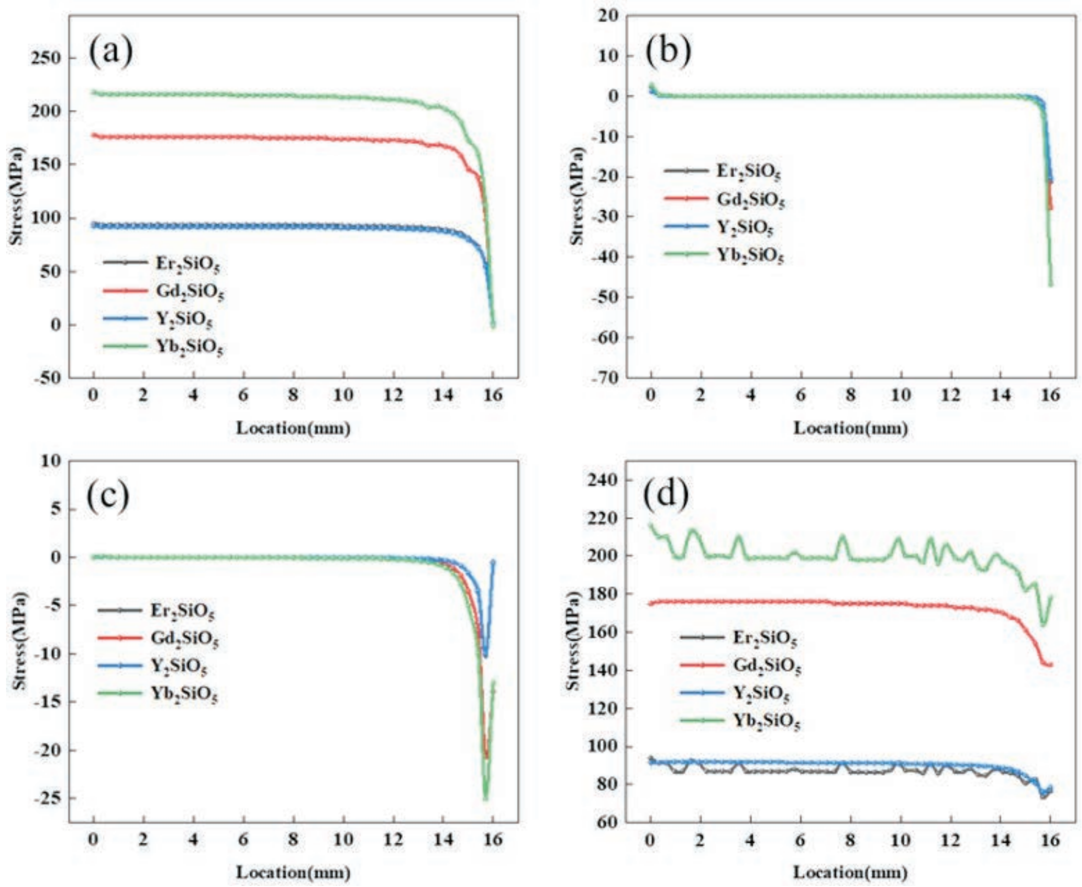

Fig. 13: Residual stress as the function of the location along the radial direction with a 110-µm top-coat for the $Yb_2SiO_5/Yb_2Si_2O_7$ interface: (a)*Sx*, (b)*Sy*, (c)*Sxy*, (d)*Seqv*.

Some experimental results have been used to verify the simulation results. Bradley T. Richards [15] has found that during cooling, residual stresses caused by the mismatch of CTE triggered cracking in the coating. During thermal cycling, delamination is initiated at the edge of the coating. This was consistent with the defined path in this mode, there is high residual stress in the top-coat and at the edge of the coating. Fig. 14, Fig. 14(a), Fig. 14(b), Fig. 14(c) and Fig. 14(d) show an SEM image of Er_2SiO_5, Gd_2SiO_5, Y_2SiO_5 and Yb_2SiO_5, respectively. It is well known that a large amount of residual stress and strain is accumulated in the coating after preparation has been completed. A large number of cracks are generated with the high stress level and these stresses can lead to growth of the cracks. It could be found that Er_2SiO_5 had fewer cracks, indicating a low stress level, which was consistent with the simulation results. Gd_2SiO_5, Yb_2SiO_5 and Y_2SiO_5 have more cracks, indicating a high stress level. Fig.14(e) shows the experiment results for residual stress, Y_2SiO_5 and Er_2SiO_5 are at a low stress level (142.6 MPa ± 4 MPa),

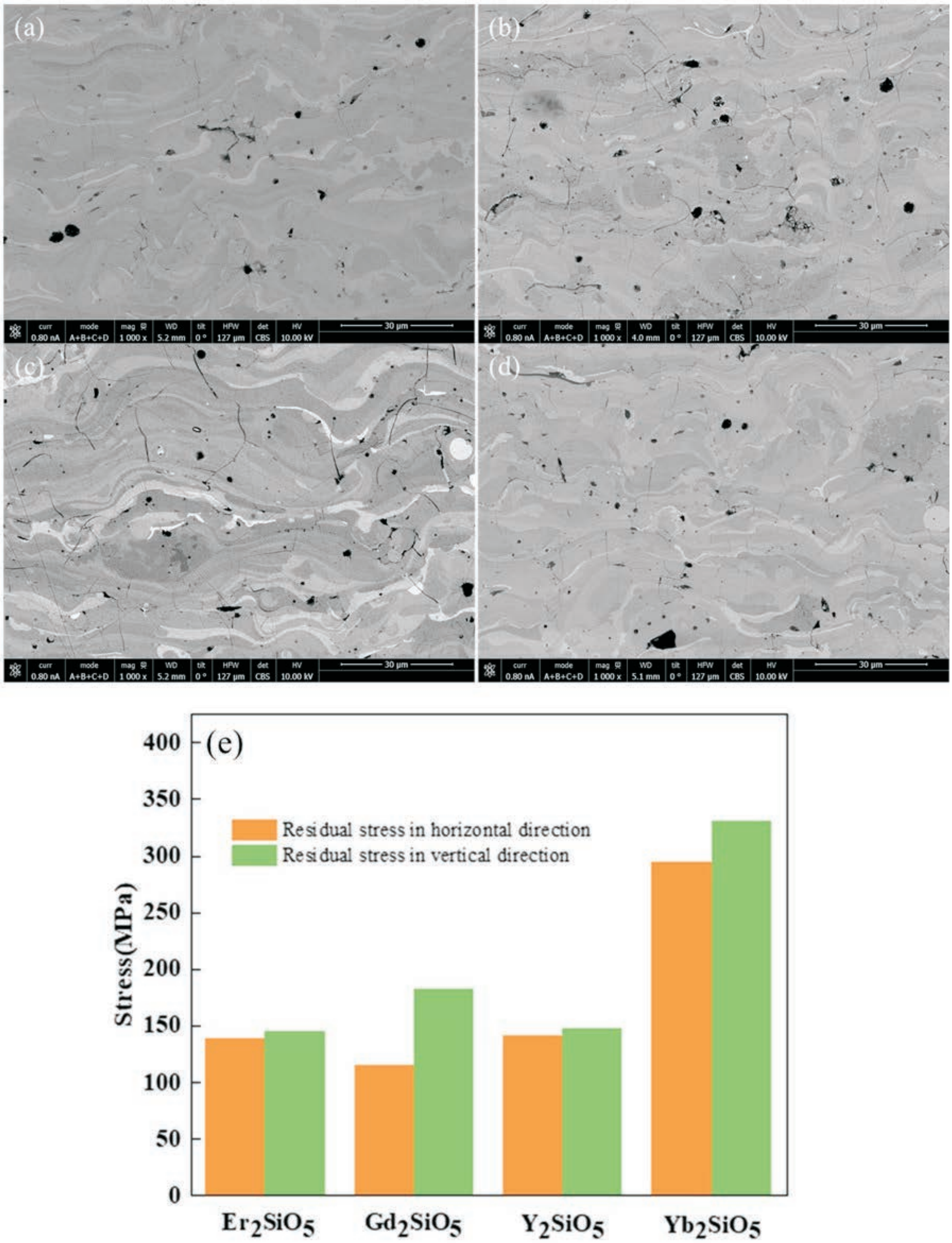

Fig. 14: Cross section image of APS-RE_2SiO_5:(a) Er_2SiO_5 (b) Gd_2SiO_5 (c) Y_2SiO_5(d) Yb_2SiO_5, (e) the results of residual stress and (f) cross-section image of the EBC system.

which is the same as the simulation. Based on combination with the above simulation results, it can be ascertained that the experimental test results are basically consistent with the CTE of the four materials, the material with the larger CTE having the higher stress. However, there are some inconsistent results in which the CTE of Gd_2SiO_5 is higher than that of Yb_2SiO_5 while the stress in Yb_2SiO_5 higher than that in Gd_2SiO_5. The same phenomenon occurs in Er_2SiO_5 and Y_2SiO_5, which indicates that the stress of the coating would be increased by the thermal conductivity, specific heat capacity and other thermophysical properties in the case of a similar CTE. Therefore, it is incomplete and incorrect to assess the magnitude of the stress only from the CTE, as the factors that affect the stress are numerous and complex. The importance of each factor is also different, and the primary factor is the CTE. But when the CTE is low, the role of other factors should be considered. The thermophysical properties of the materials should be considered comprehensively.

(3) Summary

Excessive residual stress can trigger cracks, several modes potentially damaging EBCs could be listed as: groove crack, inner arch and edge warping, as shown in Fig. 15: (1) The groove crack is mainly caused by radial tensile stress, which usually occurs in the top-coat. (2) When axial tensile stress is combined with radial compressive stress, the inner arch appears in the middle of coating. This creates a gap between the coating and the substrate, which makes the coating susceptible to breakage. (3) If axial tensile stress and radial compressive stress intersect at the edge of the coating, then edge warpage occurs. The warping of the edges facilitates the peeling off of the coating and the lifetime of the coating being significantly reduced. The crack induced by residual stress grows when the service temperature rapidly changes, this is because that the cracks are stretched by the CTE mismatch of the substrate and coatings during the temperature change. In actual service, all modes of damage occur and interact with each layer simultaneously, which results in the service lifetime of the coating being significantly reduced.

In general, increasing thickness of the top-coat promotes thermal protection of the top-coat. However, excessive thickness leads to an increase in strain. Comparative analysis of the composition of the top-coat revealed that the reason for the different residual stress of EBCs was their thermophysical parameters. The residual stress of coatings was related to their different thermophysical parameters as well as the temperature variation, which can induce high strain in the coating. Finally, based on current results, the main failure mechanisms of the coating are edge warping, as the failure process of the EBCs was described, as shown in Fig. 16. At the end of the spraying process, the sample had begun to cool and shrink, which produced the strain and residual stress. Owing to the large shrinkage of the material near the top layer, a large amount of residual stress was accumulated at the top layer and at the interfaces between the layers. Because of the edge effect, stress concentration zones were created at the coating boundary. The interaction of these two stress disruption zones led to groove cracking and edge warping of the coating. The consequence of the accumulation of radial stresses in the top-coat caused inner arching of the coating. These models will occur simultaneously after the spraying process.

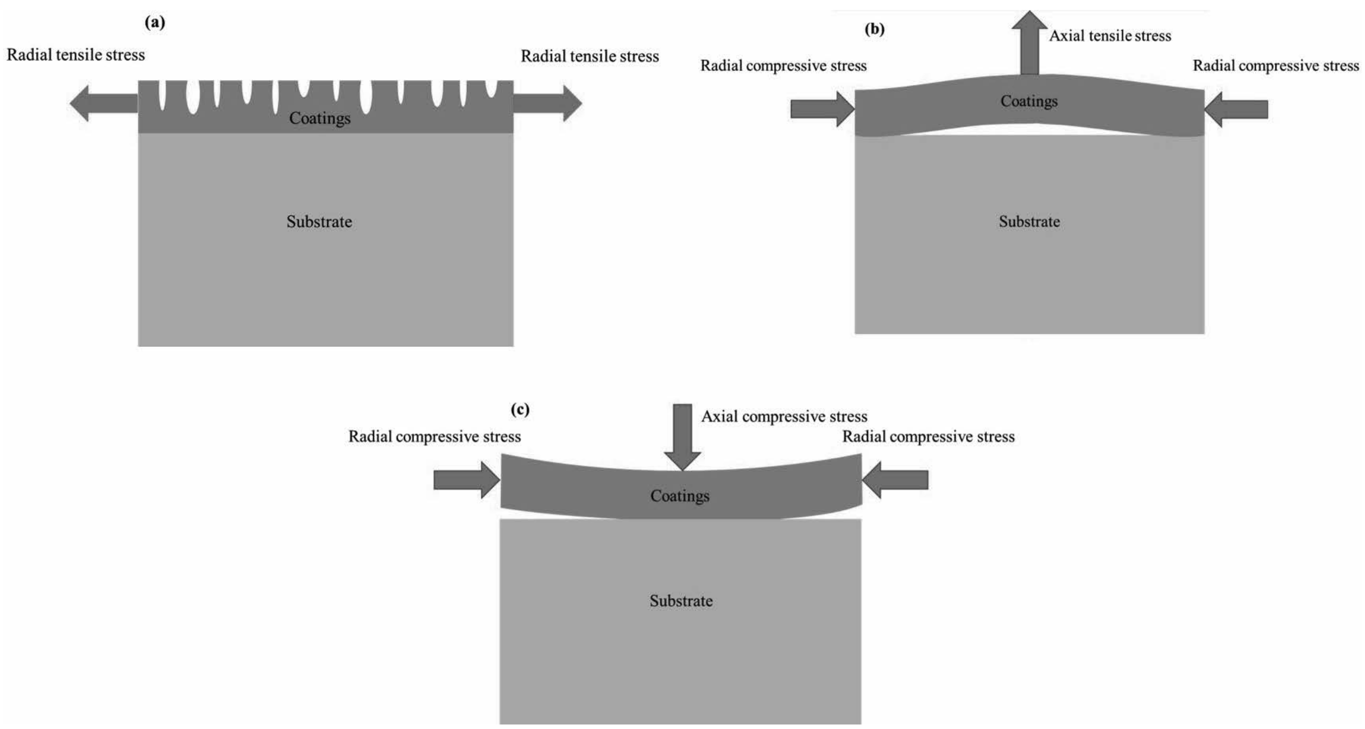

Fig. 15: Failure modes of the coating caused by residual stress:(a) Groove crack, (b) Inner arch, (c) Edge warping.

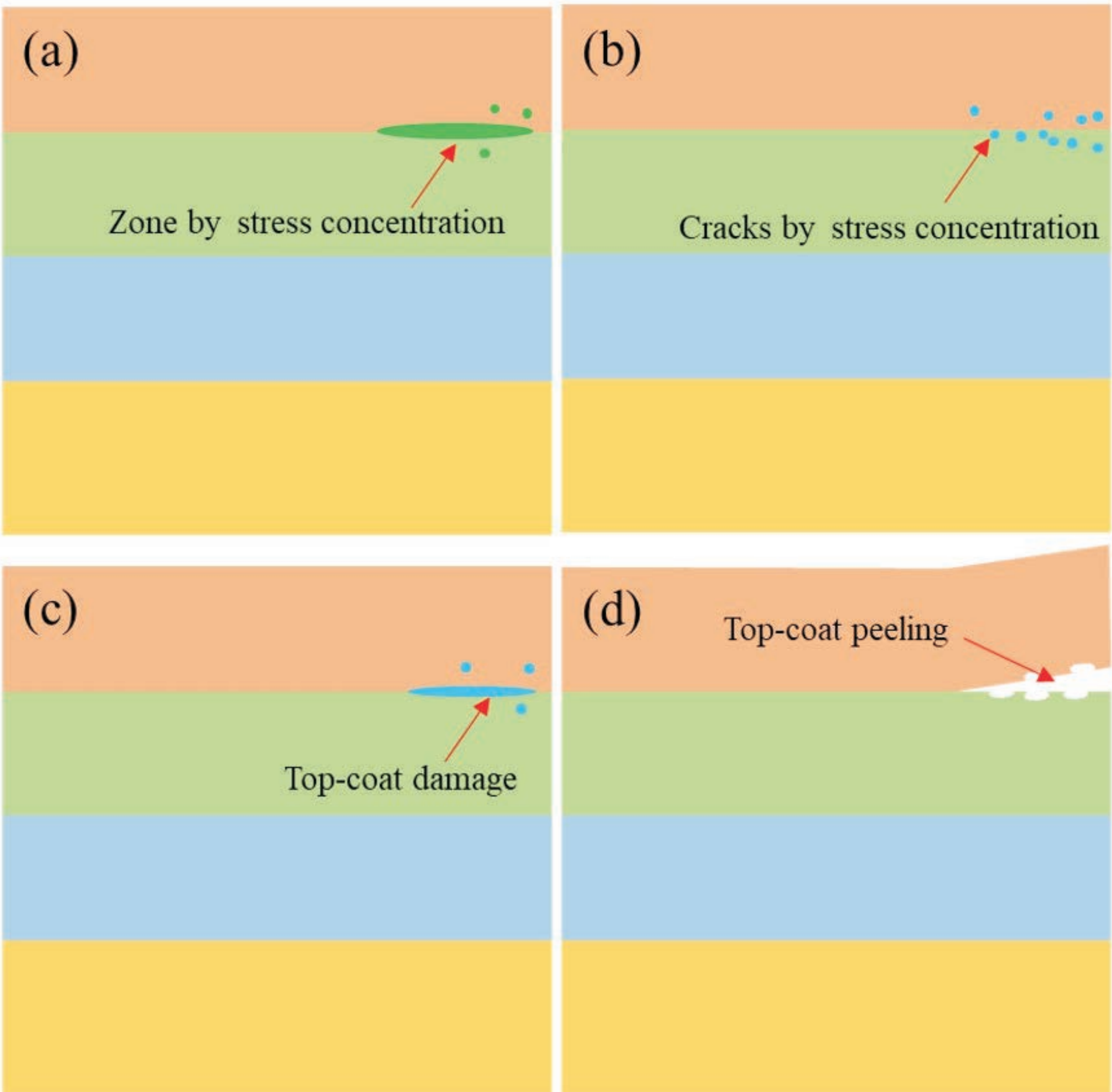

Fig. 16: Failure process of the coating caused by residual stress.

IV. Conclusions

The effect of thickness and the composition of the top-coat on the residual stress has been investigated by means of FEM. The structure of EBCs has been designed and optimized on the basis of FEM simulation, the materials that are the most suitable for the top-coat of EBCs have been selected, and the corresponding thickness has been optimized:

(1) In terms of the effect of the thickness of the coatings, the increase in thickness led to an increase in strain. Based on the stress distribution of the key interfaces in EBCs, it was found that the stress concentrations at all interfaces occurred at the edges of the coatings, and large radial stress was accumulated at the surface. The thickness of coatings had a significant impact on the interfacial stress of the coatings, which affected the quality of the coating. So, appropriate thickness helped to reduce the residual stress. Based on the current simulation results, the thickness of the top-coat for rare-earth silicate EBCs should be about 170 μm.

(2) From a comparison of the parameters of these materials, it could be seen that the thermal-physical parameters of Er_2SiO_5 and Y_2SiO_5 were more similar to those of SiC even at elevated temperatures, this was the main reason for the lower residual stress of coatings composed of Er_2SiO_5 and Y_2SiO_5. The residual stresses in Er_2SiO_5 and Y_2SiO_5 were significantly lower than those in Yb_2SiO_5 and Gd_2SiO_5, and the detailed range was Yb_2SiO_5>Gd_2SiO_5>Er_2SiO_5>Y_2SiO_5.

(3) An optimized design was proposed based on the above results, so a trilayer for APS-EBCs was Si monolithic as the bond coat, $Yb_2Si_2O_7$ as the interlayer and Y_2SiO_5 as the top-coat. The failure modes induced by residual stress for EBCs were groove crack, inner arch and edge warping.

(4) In this paper, the finite element method (FEM) has been used to design and optimize the structure of EBCs, while reducing the cost and improving the efficiency of investigations. The experimental results are consistent with most of the simulation results. The remaining inconsistent parts necessitate further research and exploration.

Acknowledgments

This research is jointly supported by the sub-project of Key Basic Research Projects of Basic Strengthening Program (Grant No. 2020-JCJQ-ZD-172 – 05), the Training Program of the Major Research Plan of the National Natural Science Foundation of China (No.91960107), the financial support of the National Natural Science Foundation of China (Nos. 51701050, 52072110, 51672067, 51541208 and 51102074), and the National NSAF (Grant No. U1730139). And this work was also supported by the Youth Innovation Promotion Association of the Chinese Academy of Sciences (Grant No.2017295), Natural Science Foundation of Shanghai (No. 19ZR1479600), the Natural Science Foundation of Hebei Province (E2018202034, E2015202070) and Basic Research of the Ministry of Science and Technology of the Chinese Academy of Sciences (CXJJ-21S029).

References

1 Kassem, R., Nasiri, N.A.: A comprehensive study on the mechanical properties of Yb2SiO5 as a potential environmental barrier coating, Surf. Coat. Technol., 426, 127783, (2021).

2 Lee, K.N., Van Roode, M.: Environmental barrier coatings enhance performance of SiC/SiC ceramic matrix composites, *Am. Ceram. Soc. Bull.*, **98**, [30],46 – 53, (2019)

3 Lee, K.N., Eldridge, J.I., Robinson R.C.: Residual stresses and their effects on the durability of environmental barrier coatings for SiC ceramics, *J. Am. Ceram. Soc.*, **88**, [12], 3483 – 3488, (2005)

4 Archer, T., Berny, M., Beauchêne, P., Beauchene, P., Hild, F.: Creep behavior identification of an environmental barrier coating using full-field measurements, *J. Eur. Ceram. Soc.*, **40**, [15], 5704 – 5718, (2020).

5 Gale, L., Harris, S., Pattison, S., Baker, J., Fowler, J.: Development and evaluation of sub-element testing of SiC/SiC ceramic matrix composites at elevated temperatures, *J. Eur. Ceram. Soc.,* **41**, [5], 3167 – 3176, (2020).

6 Bakan, E., Mack, E.D., Lobe, S., Koch, D., Vassen, R.: An investigation on burner rig testing of environmental barrier coatings for aerospace applications, *J. Eur. Ceram. Soc.,* **40**, [15], 6236 – 6240, (2020).

7 Kunz, W., Klemm, H., Michaelis, A.: Crack-healing in ytterbium silicate filled with silicon carbide particle, *J. Eur. Ceram. Soc.* **40**, [15], 5740 – 5748, (2020).

8 Chen, D., Pegler, A., Dorfman, M.: Environmental barrier coatings using low pressure plasma spray process, *J. Eur. Ceram. Soc.,* **103**, [9],4840 – 4845, (2020).

9 Chen, P., Xiao, P., Li, Z., Li, Y., Li, J.W.: Oxidation properties of tri-layer ytterbium-disilicate/mullite/silicon-carbide environment barrier coatings for C_f/SiC composites, *Surf. Coat. Technol.,* **402**, 126329, (2020).

10 Yang, H.T., Yang, Y.P., Cao, X.Q., Huang, X.Z., Li, Y.: Thermal shock resistance and bonding strength of tri-layer Yb_2SiO_5/mullite/Si coating on SiC_f/SiC composites, *Ceram. Int.,* **46**, [17], 27292 – 27298, (2020).

11 Harder, B.J., Almer, J.D., Weyant, C.M., Lee, K.N., Faber, K.T.: Residual stress analysis of multilayer environmental barrier coatings, *J. Am. Ceram.* Soc., **92**, [2], 452 – 459, (2009).

12 Liu, D., Kyaw, S.T., Flewitt, P.E.J., Seraffon, M., Simms, N.J., Pavier, M., Jones, I.A.: Residual stresses in environmental and thermal barrier coatings on curved superalloy substrates: experimental measurements and modelling, *Mater. Sci. Eng. A-Struct. Mater. Prop. Microstruct. Process.*, **606**, 117 – 126, (2014).

13 Richards, B.T., Young, K.A., Francqueville, D.F., Sehr, S., Begley, M.R., Wadley, H.N.G.: Response of ytterbium disilicate-silicon environmental barrier coatings to thermal cycling in water vapor, *Acta Mater.,* **106**, 1 – 14, (2016).

14 Harder, B.J., Almer, J.D., Weyant, C.M., Lee, K.N., Faber, K.T.: Residual stress analysis of multilayer environmental barrier coatings, *J. Am. Ceram.* Soc., **92**, [2], 452 – 459, (2009).

15 Richards, B.T., Sehr, S., Franqueville, F.D., Begley, M.R., Wadley, H.N.G.: Fracture mechanisms of ytterbium monosilicate environmental barrier coatings during cyclic thermal exposure, *Acta Mater.,* **103**, 448 – 460, (2016).

16 Zhong, X., Zhu, T., Niu, Y.R., Zhou, H.J., Zhang, L., Zhang, X.Y., Li, Q.L., Zheng, X.B.: Effect of microstructure evolution and crystal structure on thermal properties for plasma-sprayed RE_2SiO_5 (RE=Gd, Y, Er) environmental barrier coatings, *J. Mater. Sci. Technol.*, **85**, 141 – 151, (2021).

17 Lv, B.W., Jin, X.C., Cao, J., Xu, B.S., Wang, Y.G., Fang, D.N.: Advances in numerical modeling of environmental barrier coating systems for gas turbines, *J. Eur. Ceram. Soc.* 40, [9], 3363 – 3379, (2020).

18 Tejero-Martin, D., Bennett, C., Hussain, T.: A review on environmental barrier coatings: history, current state of the art and future developments, *J. Eur. Ceram. Soc.,* **41**, 1747 – 1768, (2021).

19 Lee, K.N., Waters, D.L., Puleo, B.J., Garg, A., Jennings, W.D., Costa, G., Sacksteder, D.E.: Development of oxide-based high temperature environmental barrier coatings for ceramic matrix composites via the slurry process, *J. Eur. Ceram. Soc.*, **41**, [2],1639 – 1653, (2020).

20 Padture, N.P.: Environmental degradation of high-temperature protective coatings for ceramic-matrix composites in gas-turbine engines, *NPJ Mater. Degrad.*, **39**, [7], 2409 – 2418, (2019).

21 Padture, N.P.: Advanced structural ceramics in aerospace propulsion, *Nat. Mater.,* **15**, [8], 804 – 809, (2016).

22 Pang, M., Zhang, X., Liu, Q., Fu, Y.X., Liu, G., Tan, W.D.: Effect of preheating temperature of the substrate on residual stress of Mo/8YSZ functionally gradient thermal barrier coatings prepared by plasma spraying, *Surf. Coat. Technol.*, **385**, 125377, (2020).

23 Ridley, M., McFarland, B., Miller, C., M., Opila, E.: $YbPO_4$: A novel environmental barrier coating candidate with superior thermochemical stability, *Materialia*, **21**, 101289, (2022).

24 Ye, H., Wu, L., Long, M., Lei Tao.: Numerical experimental investigation on dynamic failure characteristics of layered slate, *Blasting*, **34**, [3], 57 – 62(95), (2017).

25 Liu, X., Zhu, J.Q., Han, JC.: Numerical and experimental investigation on thermal shock failure of Y_2O_3-coated CVD ZnS infrared windows, *Int. J. Heat Mass Transf.,* **124**, 124 – 130, (2018).

26 Federer, J.I.: Alumina base coatings for protection of SiC ceramic, *J. Mater. Eng*., **12**, [2], 141 – 149, (1990).

27 Xu, H., Gong, S., Chen, L., Zhang, C.: Failure process of thermal barrier coatings under thermal and mechanical loading, *J. Beijing Univ. Aeronaut. Astronaut.,* **30**, [10], 919 – 924, (2004).

28 Zhong, X., Niu, Y.R., Li, H., Zeng, Y., Zheng, X.B., Ding, C.X., Sun, J.L.: Microstructure evolution and thermomechanical properties of plasma-sprayed Yb_2SiO_5 coating during thermal aging, *J. Am. Ceram. Soc.*, **100**, [5], 1896 – 1906, (2017).

29 Liu, X., Zhu, J., Han, J.: Numerical and experimental investigation on thermal shock failure of Y_2O_3-coated CVD ZnS infrared windows, *Int. J. Heat Mass Transf.,* **124**, 124 – 130, (2018).

30 Xu, Y., Hu, X.X., Xu, F.F., Li, K.W.: Rare earth silicate environmental barrier coatings: present status and prospective, *Ceram. Int.*, **43**, [8], 5847 – 5855, (2017).

31 Jiang, F., Cheng, L., Wang, Y.: Hot corrosion of RE_2SiO_5 with different cation substitution under calcium-magnesium-aluminosilicate attack, *Ceram. Int.,* **43**, [12], 9019 – 9023, (2017).

32 Summers, D.W., Poerschke, D.L., Park, D., Shaw, J.H., Zok, F.W., Levi, C.G.: Roles of composition and temperature in silicate deposit-induced recession of yttrium disilicate, *Acta Mater.,* **160**, 34 – 46, (2018).

33 Poerschke, D.L., Jackson, R.W., Levi, G.C.: Silicate deposit degradation of engineered coatings in gas Turbines: progress toward models and materials solutions, *Ann. Rev. Mater. Res.,* **47**, 297 – 330, (2017).

34 Lu, Y., Luo, L., Liu, J., Zhu, C., Wang, Y.G.: Failure mechanism associated with the thermally grown silica scale in environmental barrier coated C/SiC composites, *J. Am. Ceram.* Soc., **99**, [8], 2713 – 2719, (2016).

35 Wang, L., Li, D.C., Yang, J.S., Shao, F., Zhong, X.H., Zhao, H.Y., Yang, K., Tao, S.Y., Wang, Y.: Modeling of thermal properties and failure of thermal barrier coatings with the use of finite element methods: A review, *J. Eur. Ceram. Soc.*, **36**, [6], 1313 – 1331, (2016).

36 Wang, L., Shao, F., Zhong, X.H., Ni, J.X., Yang, K., Tao, S.Y., Wang, Y.: Tailoring of self-healing thermal barrier coatings via finite element method, *Appl. Surf. Sci.*, **431**, 60 – 74, (2018).